

HDW-SR: High-Frequency Guided Diffusion Model based on Wavelet Decomposition for Image Super-Resolution

Chao Yang*, Boqian Zhang*, Jinghao Xu, Guang Jiang †
Xidian University

{24011211295, 24011211294, 23011210789}@stu.xidian.edu.cn,
gjiang@mail.xidian.edu.cn

Abstract

Diffusion-based methods have shown great promise in single image super-resolution (SISR); however, existing approaches often produce blurred fine details due to insufficient guidance in the high-frequency domain. To address this issue, we propose a High-Frequency Guided Diffusion Network based on Wavelet Decomposition (HDW-SR), which replaces the conventional U-Net backbone in diffusion frameworks. Specifically, we perform diffusion only on the residual map, allowing the network to focus more effectively on high-frequency information restoration. We then introduce wavelet-based downsampling in place of standard CNN downsampling to achieve multi-scale frequency decomposition, enabling sparse cross-attention between the high-frequency subbands of the pre-super-resolved image and the low-frequency subbands of the diffused image for explicit high-frequency guidance. Moreover, a Dynamic Thresholding Block (DTB) is designed to refine high-frequency selection during the sparse attention process. During upsampling, the invertibility of the wavelet transform ensures low-loss feature reconstruction. Experiments on both synthetic and real-world datasets demonstrate that HDW-SR achieves competitive super-resolution performance, excelling particularly in recovering fine-grained image details. The code will be available after acceptance.

1. Introduction

Single Image Super-Resolution (SISR) aims to reconstruct a high-resolution (HR) image from a low-resolution (LR) input. This task has been widely applied in low-level vision. However, due to the resolution limitations of the LR image, certain details may be blurred or lost, making accurate restoration of fine details a critical challenge for SISR.

*These authors contributed equally to this work.

†Corresponding authors.

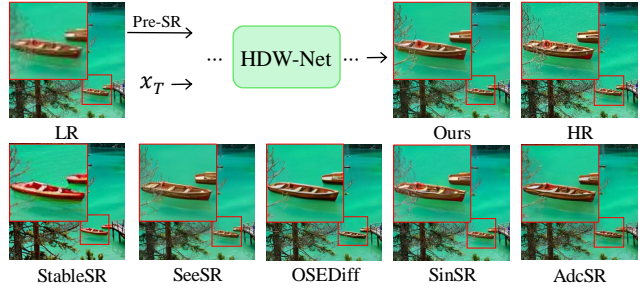


Figure 1. Existing methods achieve good performance in restoring the overall structure, but still have deficiencies in detail reconstruction (e.g. the lifebuoy on the boat).

In recent years, Generative Models have achieved advances in the SISR task, particularly in restoring high-frequency details and producing high-quality images. Compared to traditional regression methods, GAN-based methods in SISR[30] can explicitly constrain the generator's output to match the natural image distribution, thereby synthesizing more realistic SR images. Moreover, GANs readily incorporate perceptual and feature-matching losses to further enhance subjective texture fidelity. Nevertheless, training GAN-based approaches is difficult, and the convolutional upsampling operations often introduce conspicuous checkerboard artifacts in the generated HR images [48].

Compared to GANs, diffusion models can achieve better recovery of high-frequency details and texture information during the image generation process through a step-by-step denoising approach. Currently, some diffusion-based methods [16, 26, 39, 48] typically generate HR images from random noise through multiple denoising steps. This approach not only prolongs convergence, but also limits the model's ability to focus on fine-grained details, leading to texture details loss. Subsequent methods, such as Pre-trained Diffusion Models [25, 27, 37] and Residual Learning Diffusion Models [34, 48], have shown improvements in detail recovery. However, these approaches still exhibit deficiencies in

recovering local details and handling multi-scale features due to their reliance on global image features and the absence of high-frequency prior guidance.

To overcome these limitations, we propose a High-Frequency Guided Diffusion Model based on Wavelet Decomposition for Image Super-Resolution(HDW-SR). Since wavelet decomposition can losslessly separate an image into low- and high-frequency components, it avoids the high-frequency detail loss commonly caused by traditional CNN downsampling. Therefore, the model integrates wavelet transforms to extract multi-scale features and uses a pre-super-resolved (PreSR) image, which is resolved from LR image, to provide high-frequency guidance during diffusion. Specially, we first use PreSR image to generate a residual map based on the difference between PreSR image and the HR image. Subsequently, diffusion is performed based on the residual map. In the diffusion process, we replace the traditional U-Net with the High-Frequency Guided Diffusion by Wavelet Decomposition Network (HDW-Net), which utilizes the high-frequency prior guidance provided by PreSR image during the diffusion.

HDW-Net consists of two components: the High-Frequency Extraction Network (HE-Net) and the High-Frequency Augmentation Network (HA-Net). HE-Net serves as a feature extraction network that performs multi-level wavelet decomposition on the PreSR image to extract high-frequency components at different scales. By employing a U-Net-like architecture optimized with reconstruction loss, HE-Net ensures that the extracted wavelet components are precise and robust, providing reliable high-frequency guidance for the subsequent HA-Net. In HA-Net, the denoised image is processed through wavelet decomposition, which effectively separates low- and high-frequency components while preserving spatial structures, thus enhancing the model’s detail perception and reconstruction accuracy[20]. The low-frequency components obtained from wavelet decomposition and the high-frequency components extracted by HE-Net are fed into an encoder based on Dynamic Focused Attention (DFA), where sparse cross-attention computation guides the high-frequency prior. The combination of residuals and high-frequency components effectively strengthens the network’s ability to restore fine details, avoiding excessive noise or distortion.

To precisely select essential elements from the similarity matrix and enhance high-frequency guidance quality, we propose the Dynamic Thresholding Block (DTB), an enhancement over the conventional Top-K mechanism. Observing that elements in the normalized similarity matrix of the cross-attention often exhibit a bimodal distribution, DTB dynamically computes thresholds based on intra-class and inter-class variances, allowing more precise element selection. This method significantly refines the network’s

focus on high-frequency details and accelerates computational efficiency.

The main contributions of our work are as follows:

- We propose HDW-Net, a network structure that integrates wavelet transform and DFA-based high-frequency feature encoding within the diffusion framework. By replacing traditional CNN-based sampling with wavelet transforms and using the high-frequency information from the PreSR image as guidance for the diffusion process, our approach significantly enhances detail reconstruction accuracy.
- Within DFA, we propose the DTB, a module that dynamically determines data selection thresholds by analyzing the variance in similarity matrices, enabling more precise and adaptive selection of key elements.
- Extensive experiments have demonstrated that our model achieves superior performance and metrics, particularly excelling in detail restoration.

2. Related Work

Deep learning-based methods have become the mainstream approach for SISR. The application of CNNs and Transformer [35] has significantly enhanced SISR performance [17, 19, 47, 49, 53]. The Residual Dense Network (RDN) [54], by incorporating local and global feature fusion mechanisms within multiple residual dense blocks, effectively exploits multi-level information. The Progressive Focused Transformer (PFT) [22], utilizing a sparse attention mechanism, improves the SISR performance while reducing computational complexity. Furthermore, significant advancements have been made in generative-model-based SISR methods, which can be broadly categorized into GAN-based approaches [18, 30, 52] and diffusion-based methods [4, 16, 41].

2.1. Diffusion-based SISR

Recently, diffusion models have made significant progress in the field of image generation [9, 14] and have gradually been applied to SISR reconstruction tasks, Gendy’s work [11] provides a summary of the application of diffusion models in image super-resolution. Methods based on generative priors have achieved notable success with Stable Diffusion [31, 32]. For instance, ResShift [48] effectively reduces denoising steps by shortening the Markov chain, while ResDiff [33] significantly improves the reconstruction accuracy of high-frequency details within a frequency-domain-guided framework. Single-step diffusion-based SISR methods [5, 43, 46] achieve performance comparable to multi-step methods with far fewer sampling steps. However, existing methods often still suffer from issues of excessive smoothing or artifact introduction in high-frequency regions, necessitating more refined attention mechanisms and prior fusion strategies to enhance SISR performance.

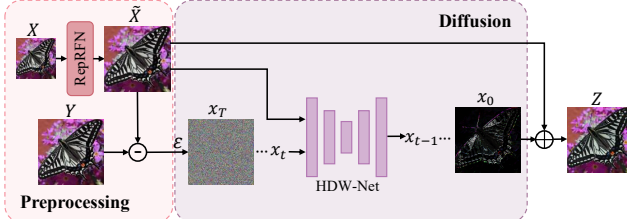


Figure 2. Overview of Prior-based Residual Diffusion Network.

2.2. Wavelet transform for SISR

Wavelet decomposition [7] combined with deep learning techniques [2, 13, 45, 55] has made significant progress in the field of SISR. The Lifting Wavelet-Guided Diffusion Model [29] improves image super-resolution accuracy and efficiency by restoring details in the wavelet domain. However, its performance is limited by the diffusion model's struggle to distinguish between details and noise during denoising, affecting reconstruction quality. DiWa [24] transfers the diffusion process to the wavelet domain. But frequency-domain diffusion depends on input image quality, and the lack of residual learning hinders precise detail recovery. Therefore, our work applies the wavelet transform to the residual diffusion process, utilizing the transform to inject multi-scale high-frequency information, enabling more accurate recovery of high-frequency details and thus achieving SISR in the image domain.

3. Method

This chapter elaborates on the HDW-SR architecture. In Section 3.1, we present the overall structure of the HDW-SR. Section 3.2 discusses the design of the HDW-Net. Finally, in Section 3.3, we provide a detailed explanation of the encoder design based on the DFA mechanism with dynamic thresholding.

3.1. Prior-based Residual Diffusion Network

The detailed design of the network is shown in Figure 2. We consider image pairs $(X_i, Y_i) \in \mathcal{D}$, where $X_i \in \mathbb{R}^{H \times W \times 3}$ is the LR image and $Y_i \in \mathbb{R}^{H \times W \times 3}$ is the HR image. To make the network more focused on learning high-frequency information and reduce training costs, we perform diffusion on the residuals: First, the lightweight CNN network RepRFN [8] is used to preprocess X_i , and the PreSR image $\tilde{X}_i \in \mathbb{R}^{H \times W \times 3}$ is subtracted from Y_i to obtain the residual image $\Delta X_i \in \mathbb{R}^{H \times W \times 3}$ which narrows the dynamic range of the signal that the model must learn. By progressively adding noise to ΔX_i , we obtain the pure noise sample x_T . During the subsequent reverse denoising process, the PreSR \tilde{X}_i serves as a guidance signal and, together with the noise sequence $x_t, t = 0 \dots T$, is fed into HDW-Net to predict the residual map $\Delta X_{\theta,i}$. Finally, adding $\Delta X_{\theta,i}$ to \tilde{X}_i yields

the super-resolved image $Z_i \in \mathbb{R}^{H \times W \times 3}$.

3.2. HDW-Net

HDW-Net replaces CNN-based downsampling and upsampling operations with wavelet transforms to process the noise x_t and the PreSR \tilde{X}_i . The high-frequency wavelet components decomposed from \tilde{X}_i are employed as guidance throughout the diffusion process. As shown in Figure 3, HDW-Net consists of two sub-networks: the HE-Net and the HA-Net.

3.2.1. HE-Net

As shown in the left panel of Figure 3, the input image \tilde{X} undergoes multi-level downsampling using the Haar wavelet [12]. In the j -th sampling step, the image \tilde{x}^{j-1} , $j = 1, 2, 3$ is decomposed into four subbands based on the Haar wavelet basis.

$$\text{2D-DWT}(\tilde{x}^{j-1}) = \tilde{x}^{j,LL}, \tilde{x}^{j,LH}, \tilde{x}^{j,HL}, \tilde{x}^{j,HH}, \quad (1)$$

The term $\tilde{x}^{j,LL}$ represents the low-frequency component that captures the structural features of the image. After a convolutional operation adjusts its channel dimension, the resulting \tilde{x}^j is used for next-level wavelet downsampling. The set $\tilde{x}^{j,LH}, \tilde{x}^{j,HL}, \tilde{x}^{j,HH}$ corresponds to the high-frequency components, collectively denoted as $\tilde{x}^{j,H}$ in the following discussion. These components extract fine-grained details of the image and serve as high-frequency guidance, fed into the corresponding layers of HA-Net during the denoising process. Repeating this procedure iteratively, the final low-frequency component $\tilde{x}^{3,LL}$ is passed through a fully connected (FC) layer to produce the enhanced feature $\tilde{x}_{\theta}^{3,LL}$, which initializes the low-frequency wavelet component for the upsampling process. Subsequently, the low-frequency component at each level, together with its corresponding high-frequency component, is progressively reconstructed through the inverse wavelet transform: $\tilde{x}_{\theta}^{j-1} = \text{2D-IDWT}(\tilde{x}_{\theta}^{j,LL}, \tilde{x}^{j,H})$.

After completing the final upsampling step, a CNN is used to obtain the output \tilde{X}_{θ} . The loss function \mathcal{L}_{HE} is applied to constrain the HE-Net, ensuring high-quality restoration of \tilde{X}_i and providing accurate high-frequency guidance for the HA-Net. The loss \mathcal{L}_{HE} is defined as follows:

$$\mathcal{L}_{HE} = \left\| \tilde{X} - \tilde{X}_{\theta} \right\|_2 + \left\| \tilde{X} - \tilde{X}_{\theta} \right\|_1, \quad (2)$$

3.2.2. HA-Net

The diffusion process is illustrated on the right side of Figure 3, where x_t is fed into HA-Net and passed through convolution layers to align its channel dimensions with those of HE-Net, yielding x_t^0 . Similarly, for the j -th layer sampling, Haar wavelet downsampling is first applied:

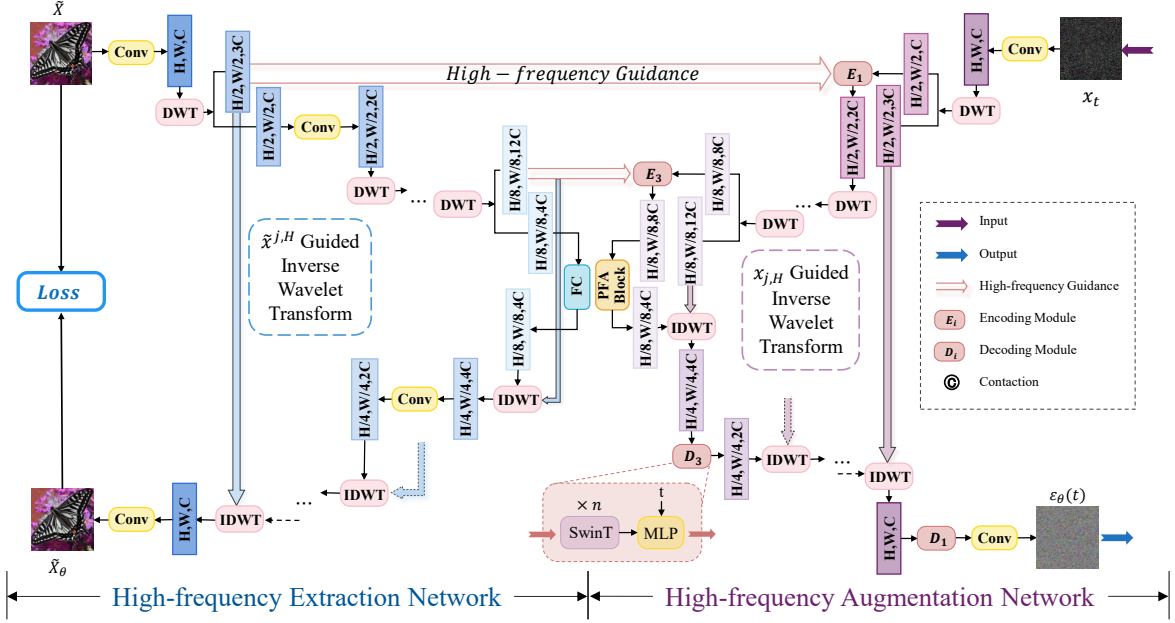


Figure 3. Overview of HDW-Net. HE-Net extracts the high-frequency component of \tilde{X} and feeds it into the HA-Net on the right. The HA-Net encoder then computes cross-attention between high- and low-frequency components to extract detailed features, completing the diffusion process.

$$\text{2D-DWT}(x_t^{j-1}) = x_t^{j,LL}, x_t^{j,LH}, x_t^{j,HL}, x_t^{j,HH}. \quad (3)$$

From x_t^{j-1} ($j = 1, 2, 3$), four subbands are obtained through wavelet downsampling, including the low-frequency subband $x_t^{j,LL}$ and the high-frequency subband $x_t^{j,H}$. The downsampling mechanism of the wavelet transform prevents the high-frequency information loss commonly caused by traditional pooling, particularly in regions rich in edges or textures. Compared with other frequency-domain methods, the wavelet transform provides a joint space-frequency localized representation, which is more suitable for optimizing high-frequency details in super-resolution tasks. The low-frequency subband $x_t^{j,LL}$ and the corresponding high-frequency component $\tilde{x}_t^{j,H}$ from HE-Net are jointly fed into the encoding module E_j (to be detailed in Section 3.3). The PreSR \tilde{X}_i provides high-frequency guidance for the diffusion process, formulated as $x_t^{j+1} = \mathcal{E}(x_t^{j,LL}, \tilde{x}_t^{j,H})$. Repeating this process iteratively, the output x_t^3 of the final encoding module is passed through the Progressive Sparse Attention (PFA) module to obtain $x_{t,\theta}^{3,LL}$.

In the upsampling stage, we use $x_t^{j,H}$ instead of $\tilde{x}_t^{j,H}$ as the high-frequency component for the inverse wavelet transform. This design choice stems from the observation that, at the early diffusion stages, the high-frequency prior of \tilde{X} provides strong guidance for detail restoration

in x_t ; however, as t gradually decreases toward 0, x_t becomes increasingly rich in high-frequency details. Excessive reliance on \tilde{X} at this point would amplify pseudo-details and distort textures, thereby hindering further refinement of high-frequency quality. The upsampling process is then repeated as follows: $x_{t,\theta}^{j-1} = \text{2D-IDWT}(x_{t,\theta}^{j,LL}, x_{t,\theta}^{j,H})$, $x_{t,\theta}^{j-1,LL} = \mathcal{D}(x_{t,\theta}^{j-1})$, where \mathcal{D} denotes the decoder composed of n Swin-T layers and an MLP block (the former enhances high-dimensional features, while the latter embeds the timestep t). The final predicted diffusion noise $\varepsilon_\theta(x_t, t)$ is then used to compute the HA-Net loss \mathcal{L}_{HA} :

$$\mathcal{L}_{HA} = \mathbb{E}_\theta \|\varepsilon_t - \varepsilon_\theta(x_t, t)\|^2. \quad (4)$$

We define the overall loss function of the network as \mathcal{L} :

$$\mathcal{L} = \beta \mathcal{L}_{HE} + (1 - \beta) \mathcal{L}_{HA}, \quad (5)$$

Here, β is a hyperparameter, and in this network, we set $\beta = 0.2$.

3.3. DFA-Based Encoder

Motivated by PFA[22], we design a DFA-Based encoder using a dynamic-threshold sparse attention mechanism for efficient high-frequency guidance. In E_j , the $x_t^{j,LL}$ is first enhanced through two layers of Swin-Transformer [21]. Subsequently, the enhanced low-frequency feature (used as

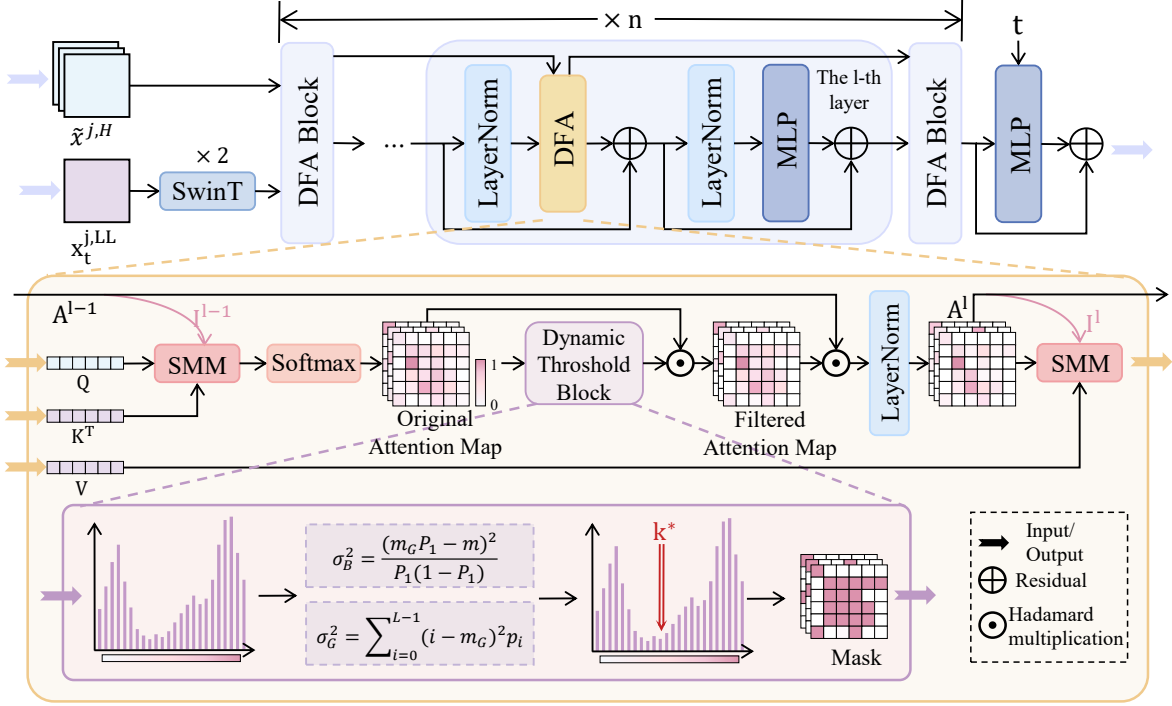


Figure 4. Overview of the DFA-based encoder: DFA performs sparse cross-attention between low- and high-frequency wavelet components, while DTB dynamically selects K via inter-class and intra-class variances, supplanting Top-K.

Q) and the corresponding high-frequency guidance feature $\tilde{x}^{j,H}$ (used as both K and V) are jointly fed into the DFA module to perform cross-attention between high- and low-frequency representations.

Here, we introduce a sparse matrix multiplication (SMM), denoted as “ Ψ ” to reduce computational complexity; it also performs sparse indexing based on the previous layer’s attention indices $I^{l-1} \in \mathbb{R}^{N \times N}$:

$$A_{\text{oam}}^l = \text{Softmax}(\Psi(Q^l, (K^l)^\top, I^{l-1})) \quad (6)$$

The update rule for the sparse indexing matrix is $I^l = \text{Sign}(A^l)$.

Due to the significant difference between $x_t^{j,LL}$ and $\tilde{x}^{j,H}$, the values in A_{oam}^l often exhibit a bimodal distribution. Based on this observation, we propose the Dynamic Thresholding Block (DTB), which adaptively determines the Top- K threshold in sparse attention. Specifically, the element values $a_{i,j}$ in A_{oam}^l are organized into a histogram over the range $[0, 1]$ with intervals of $1/512$, as shown in Figure 4.

We divide $a_{i,j}$ into two categories based on a variable threshold $T(k) = k$: class C_1 contains the elements within the interval $[0, k]$, while the remaining elements are assigned to class C_2 . Following the computation of intra-class variance $\sigma_c^2(k)$ and inter-class variance $\sigma_B^2(k)$ in image thresholding[28], the optimal threshold k^* is determined as

$$k^* = \arg \max_k \sigma_B^2(k).$$

Based on the optimal threshold k^* , the elements in A_{oam}^l greater than k^* are set to 1, and the remaining elements are set to 0, resulting in the dynamic MASK. By element-wise multiplication with MASK, the elements in A_{oam}^l are selectively filtered in a more flexible manner, yielding A_{fam}^l .

The attention map for the current layer is:

$$A^l = \text{Norm}(A^{l-1} \odot A_{\text{fam}}^l). \quad (7)$$

By incorporating the previous layer’s attention map A^{l-1} from the previous layer, high-frequency guiding information is propagated through successive multiplications. Subsequently, the output of the current layer is computed using Ψ :

$$O^l = \Psi(A^l, V^l, I^l). \quad (8)$$

This completes a sign DFA operation. By iterating the DFA block n times, cross-attention guidance is established from $\tilde{x}^{j,H}$ to $x_t^{j,LL}$, thereby fulfilling the functionality of the encoder module. Thanks to dynamic-threshold sparse attention and layer-wise weights propagation, the DFA-based encoder reduces computational complexity while accurately preserving and enhancing cross-layer consistent high-frequency key information. This facilitates the extraction of more discriminative fine-grained features for subsequent reconstruction.

Datasets	Methods	Publication	PSNR↑	SSIM↑	LPIPS↓	DISTS↓	NIQE↓	CLIPQA↑	MUSIQ↑
DIV2K	ResShift	NeurIPS'2023	24.69	0.6175	0.3374	0.2215	6.82	0.6089	60.92
	StableSR	IJCV'2024	23.31	0.5728	0.3129	0.2138	4.76	0.6682	65.63
	SeeSR	CVPR'2024	23.71	0.6045	0.3207	0.1967	5.83	<u>0.6857</u>	68.49
	SinSR	CVPR'2024	24.43	0.6012	0.3262	0.2066	6.02	0.6499	62.80
	OSEDiff	NeurIPS'2024	23.72	0.6108	0.2941	0.1976	4.71	0.6693	67.97
	AdcSR	CVPR'2025	23.62	0.6052	0.3062	0.1994	4.82	0.6594	69.37
	DiT-SR	AAAI'2025	24.31	0.6074	<u>0.2913</u>	<u>0.1956</u>	<u>4.55</u>	0.6711	<u>69.47</u>
	Ours	-	<u>24.52</u>	<u>0.6162</u>	0.2823	0.1934	4.43	0.6937	69.68
RealSR	ResShift	NeurIPS'2023	26.31	0.7411	0.3489	0.2498	7.27	0.5450	58.10
	StableSR	IJCV'2024	24.69	0.7052	0.3091	0.2167	5.76	0.6195	65.42
	SeeSR	CVPR'2024	25.33	0.7273	0.2985	0.2213	5.38	0.6204	<u>69.37</u>
	SinSR	CVPR'2024	<u>26.30</u>	0.7354	0.3212	0.2346	6.31	0.6594	60.41
	OSEDiff	NeurIPS'2024	25.15	0.7341	0.2921	<u>0.2128</u>	<u>5.37</u>	0.6693	69.09
	AdcSR	CVPR'2025	24.92	0.7284	0.3006	0.2216	5.61	0.6594	69.17
	DiT-SR	AAAI'2025	25.31	0.7337	0.2863	0.2181	5.36	0.6961	65.83
	Ours	-	25.71	0.7428	<u>0.2672</u>	0.2044	5.39	<u>0.6702</u>	70.10
DrealSR	ResShift	NeurIPS'2023	28.45	0.7632	0.3489	0.2498	8.28	0.5259	49.86
	StableSR	IJCV'2024	28.04	0.7460	0.3354	0.2287	6.51	0.6167	58.50
	SeeSR	CVPR'2024	28.26	0.7698	0.3197	0.2306	6.52	0.6672	64.84
	SinSR	CVPR'2024	28.41	0.7495	0.3741	0.2488	7.02	0.6367	55.34
	OSEDiff	NeurIPS'2024	27.92	0.7835	0.2968	0.2165	6.49	<u>0.6963</u>	64.65
	AdcSR	CVPR'2025	28.10	0.7726	<u>0.3046</u>	0.2200	6.45	0.6849	<u>66.26</u>
	DiT-SR	AAAI'2025	28.17	0.7792	0.3015	<u>0.2164</u>	<u>6.31</u>	0.6920	<u>65.74</u>
	Ours	-	<u>28.43</u>	0.7824	0.2960	0.2153	6.20	0.6970	66.36

Table 1. Quantitative comparison among the state-of-the-art DM-based SR methods on synthetic and real-world test datasets. The best and second-best results are in **bold** and underlined, respectively.

4. Experiments

4.1. Experiments Settings

4.1.1. Experiments Environment.

The proposed model was trained on a workstation equipped with an Intel Core i9-14900 CPU and dual NVIDIA RTX 4090 GPUs, running Ubuntu 22.04. The implementation utilized PyTorch 2.0.1 with CUDA 11.8. For training, low-resolution (LR) and high-resolution (HR) image pairs from the DIV2K and LSDIR datasets were employed, incorporating a $4\times$ upsampling factor. In the network architecture, the DFA module was repeated [2, 4, 4] times across its three respective stages, while the Swin-T decoder consisted of [4, 6, 6] repeated layers. Model optimization was conducted using the Adam optimizer with an initial learning rate of 1×10^{-4} , over a total of 100,000 training iterations.

4.1.2. Compared methods.

We compare HDW-SR with multi-step DM-based methods StableSR [37], ResShift [48], SeeSR [44], one-step DM-based methods SinSR [39], OSEDiff [43], AdcSR [5] and the DiT-based method DiT-SR [6]. All comparative results are obtained using officially released codes or models.

4.1.3. Test datasets and evaluation metrics.

Following previous work[43, 44], we evaluate all methods on both synthetic and real-world datasets. The synthetic dataset consists of 3,000 images of size 512×512 cropped from DIV2K[1]. The real-world images are center-cropped from RealSR[3] and DrealSR[42]. PSNR and SSIM[40] are used to measure the fidelity of SR images; LPIPS[51] and

DISTS[10] are used to assess the perceptual quality of SR; NIQE[23], CLIPQA[36], and MUSIQ[15] evaluate image quality without reference images.

4.2. Comparisons with State-of-the-Arts

4.2.1. Comparison Results on the Synthetic DIV2K Dataset

The upper part of Table 1 and Figure 5 present the comparison results of HDW-SR with other diffusion-based methods on the DIV2K dataset. ResShift achieves good PSNR and LPIPS results but struggles to recover rich details in generated images. StableSR and SeeSR utilize Stable Diffusion priors and high-level semantics to recover global structures, but they suffer from noticeable artifacts (e.g., shadows on glass). OSEDiff compresses the diffusion process into one-step inference for greater efficiency, yet its outputs omit many fine details. AdcSR accelerates generation via distillation but produces overly smooth results with weak detail recovery. SinSR performs poorly across most metrics and yields visually unnatural outputs. DiT-SR benefits from the DiT backbone's strong capacity, yielding good quantitative scores; however, it tends to over-enhance textures (e.g., distorted dust grilles on car fronts). In contrast, HDW-SR delivers superior visual quality and structural fidelity. Its lossless wavelet sampling and high-frequency guidance module align the reconstructed structures closely with the HR images. Additionally, the DTB module further refines the guidance, enabling precise and natural recovery of fine details.

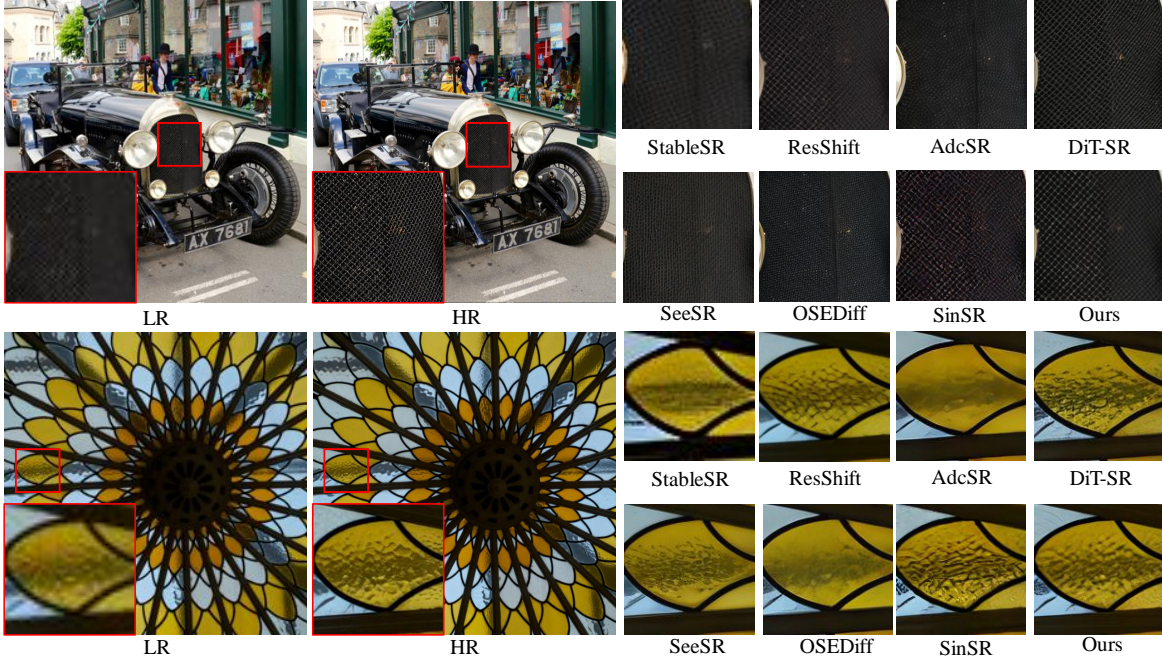


Figure 5. Visual comparisons of different DM-based SR methods on DIV2K.

4.2.2. Comparison Results on Real-World Datasets

The lower half of Table 1 and Figure 6 compare HDW-SR with other diffusion-based methods on real-world datasets. StableSR and SeeSR exhibit poor performance in both quantitative metrics and visual quality, suffering from noticeable distortions and edge blurring. ResShift still fails to reconstruct rich, coherent details, limiting perceptual quality. Although OSEDiff and AdcSR improve inference speed, they compromise high-frequency detail restoration (e.g., window contours). DiT-SR and SinSR produce noticeable artifacts in window regions, indicating hallucinations within the network. In contrast, HDW-SR excels in no-reference metrics and demonstrates superior capability in reconstructing intricate details such as subtle variations (e.g., the cavity in the bottom image of Figure 6). This advantage is attributed to our high-frequency guidance mechanism and the DTB, which effectively mine and preserve fine-grained image information throughout the diffusion process.

4.3. Comparisons with GAN-based Methods

Table 2 presents a comparison of HDW-SR with three state-of-the-art GAN-based methods: RealESRGAN[38], BSRGAN[50], and LDL[18], on both real-world and synthetic datasets. HDW-SR achieves the best performance on no-reference metrics including NIQE, CLIPQA, and MUSIO, while also demonstrating strong results in PSNR and LPIPS, striking a favorable balance between perceptual quality and content fidelity.

Table 2. Comparison of HDW-SR with state-of-the-art GAN-based methods on DIV2K, RealSR, and Drealsr datasets.

Datasets	Methods	PSNR \uparrow	LPIPS \downarrow	NIQE \downarrow	CLIPQA \uparrow	MUSIO \uparrow
DIV2K	RealESRGAN	24.29	0.3112	4.68	0.5577	61.06
	BSRGAN	24.38	0.3351	4.75	0.5091	61.20
	LDL	23.83	0.3256	4.85	0.5180	60.04
	HDW-SR	24.52	0.2823	4.43	0.6927	69.68
RealSR	RealESRGAN	25.69	0.2727	5.83	0.4449	60.18
	BSRGAN	26.39	0.2673	5.66	0.5001	63.21
	LDL	25.28	0.2766	6.00	0.4477	60.82
	HDW-SR	25.71	0.2672	5.39	0.6702	70.10

Table 3. Ablation results on the impact of hyperparameter β on the DIV2K dataset. Red values indicate the baseline (best) performance. Degradation percentages are approximate and align with observed drops.

β	PSNR \uparrow	SSIM \uparrow	NIQE \downarrow	CLIPQA \uparrow
0.2	24.52	0.6162	4.43	0.6937
0.1	18.39	0.4622	5.76	0.4856
0.3	23.29	0.5854	4.65	0.6243
0.4	22.07	0.5546	5.09	0.5896
0.5	10.30	0.2835	8.86	0.2012

4.4. Ablation study

4.4.1. Ablation Study on Sensitivity to β

To investigate the sensitivity of our model to the hyperparameter β (which controls the trade-off between perceptual quality and fidelity in the diffusion process), we conducted an ablation study on the DIV2K dataset. We varied β from

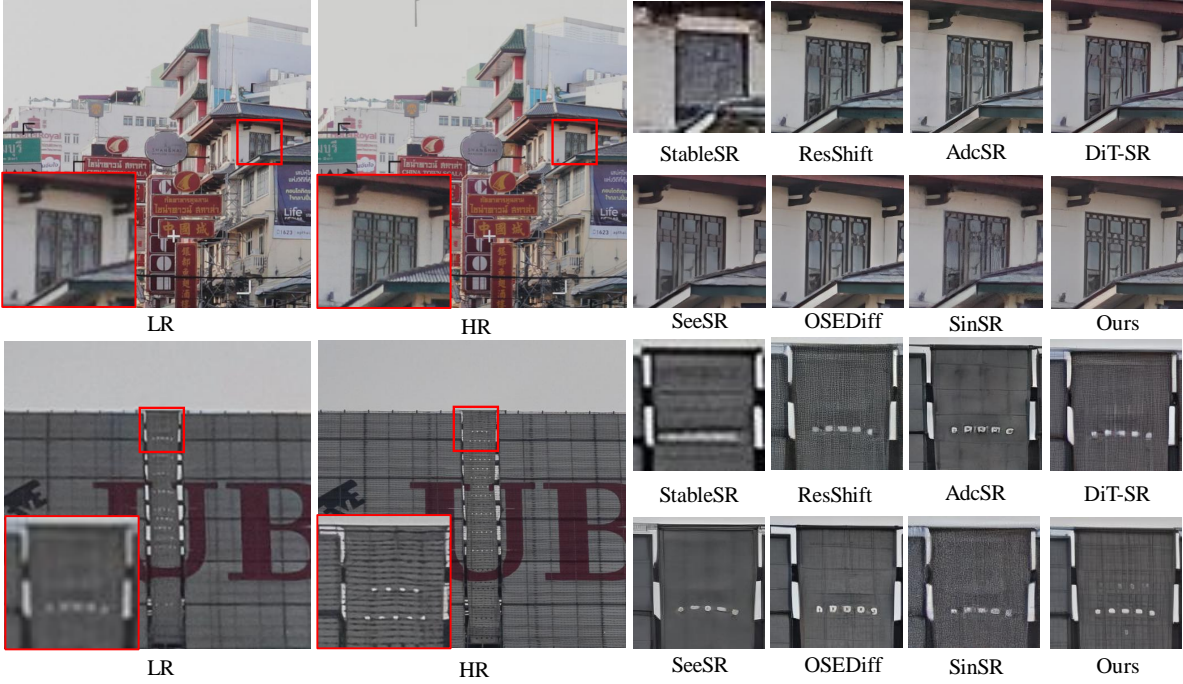


Figure 6. Visual comparisons of different DM-based SR methods on RealSR and DRealSR.

0.1 to 0.5 and observed its impact on key metrics. As shown in Table 3, at $\beta = 0.1$, all metrics degrade by 20–30%; at $\beta = 0.3$ –0.4, the degradation is limited to 5–15%; and at $\beta \geq 0.5$, the performance collapses, indicating instability in the model. This suggests an optimal range around $\beta = 0.2$ –0.3 for balancing performance.

4.4.2. Ablation Studies on Components of HDW-Net

Our ablation studies are conducted under 4 \times super-resolution on the RealSR dataset to explore the impact of each component in HDW-Net, by evaluating the effectiveness of the proposed DFA and DTB modules and comparing DWT with CNN. The results of the DWT and DFA validation are shown in Table 4. The first and last rows of Table 4 show that DWT significantly improves network performance compared to standard CNN. The last three rows compare three variants: (1) removing the DFA module and replacing it with a self-attention module, (2) using high-frequency guidance from HA-Net, and (3) generating the guidance internally within HE-Net. The comparison confirms the effectiveness of the high-frequency guidance provided by HE-Net. The results in Table 5 reveal that, compared to the Top-K, DTB better guides high-frequency information and performs more precise data selection.

5. Conclusion

In this paper, we propose HDW-SR, a diffusion-based framework for SISR that tackles the challenge of recov-

Table 4. Ablation Study of CNN and DFA Models.

Methods	PSNR \uparrow	SSIM \uparrow	CLIPQA \uparrow
CNN+DFA(HE-Net)	25.16	0.7252	0.6631
DWT+SwinT	22.15	0.6539	0.6127
DWT+DFA(HA-Net)	24.39	0.6984	0.6541
DWT+DFA(HE-Net)	25.71	0.7428	0.6702

Table 5. Ablation Study of DTB.

Methods	PSNR \uparrow	SSIM \uparrow	CLIPQA \uparrow	FLOPS
Top-K	25.37	0.7370	0.6629	172G
DTB	25.71	0.7428	0.6702	134G

ering fine details. The HDW-Net employs wavelet decomposition instead of convolution for downsampling. It also fuses the high-frequency wavelet components of the PreSR image with the low-frequency wavelet components of the diffusion noise via sparse cross-attention, thereby achieving high-frequency guidance. To further concentrate on fine details, we propose the DTB that dynamically selects the optimal threshold k^* by analyzing the intra- and inter-class variances of elements in the similarity matrix. Moreover, HDW-Net readily supports wavelet decompositions beyond the three-level configuration, such as four- and five-level decompositions, further enhancing its flexibility. Experimental results demonstrate that the proposed method effectively balances pixel-level accuracy and perceptual quality, yielding substantial gains in detail reconstruction.

References

[1] Eirikur Agustsson and Radu Timofte. Ntire 2017 challenge on single image super-resolution: Dataset and study. In *Proceedings of the IEEE conference on computer vision and pattern recognition workshops*, pages 126–135, 2017. 6

[2] Lorenzo Aloisi, Luigi Sigillo, Aurelio Uncini, and Danilo Comminiello. A wavelet diffusion gan for image super-resolution. *arXiv preprint arXiv:2410.17966*, 2024. 3

[3] Jianrui Cai, Hui Zeng, Hongwei Yong, Zisheng Cao, and Lei Zhang. Toward real-world single image super-resolution: A new benchmark and a new model. In *Proceedings of the IEEE/CVF international conference on computer vision*, pages 3086–3095, 2019. 6

[4] Wentao Chao, Junli Zhao, Fuqing Duan, and Guanghui Wang. Lfsrdiff: Light field image super-resolution via diffusion models. In *ICASSP 2025-2025 IEEE International Conference on Acoustics, Speech and Signal Processing (ICASSP)*, pages 1–5. IEEE, 2025. 2

[5] Bin Chen, Gehui Li, Rongyuan Wu, Xindong Zhang, Jie Chen, Jian Zhang, and Lei Zhang. Adversarial diffusion compression for real-world image super-resolution. In *Proceedings of the Computer Vision and Pattern Recognition Conference*, pages 28208–28220, 2025. 2, 6

[6] Kun Cheng, Lei Yu, Zhijun Tu, Xiao He, Liyu Chen, Yong Guo, Mingrui Zhu, Nannan Wang, Xinbo Gao, and Jie Hu. Effective diffusion transformer architecture for image super-resolution. In *Proceedings of the AAAI Conference on Artificial Intelligence*, pages 2455–2463, 2025. 6

[7] Ingrid Daubechies. Orthonormal bases of compactly supported wavelets. *Communications on pure and applied mathematics*, 41(7):909–996, 1988. 3

[8] Weijian Deng, Hongjie Yuan, Lunhui Deng, and Zeng-tong Lu. Reparameterized residual feature network for lightweight image super-resolution. In *Proceedings of the IEEE/CVF conference on computer vision and pattern recognition*, pages 1712–1721, 2023. 3

[9] Prafulla Dhariwal and Alexander Nichol. Diffusion models beat gans on image synthesis. *Advances in neural information processing systems*, 34:8780–8794, 2021. 2

[10] Keyan Ding, Kede Ma, Shiqi Wang, and Eero P Simoncelli. Image quality assessment: Unifying structure and texture similarity. *IEEE transactions on pattern analysis and machine intelligence*, 44(5):2567–2581, 2020. 6

[11] Garas Gendy, Guanghui He, and Nabil Sabor. Diffusion models for image super-resolution: State-of-the-art and future directions. *Neurocomputing*, 617:128911, 2025. 2

[12] Alfred Haar. *Zur theorie der orthogonalen funktionensysteme*. Georg-August-Universitat, Gottingen., 1909. 3

[13] Wei-Yen Hsu and Pei-Wen Jian. Detail-enhanced wavelet residual network for single image super-resolution. *IEEE Transactions on Instrumentation and Measurement*, 71:1–13, 2022. 3

[14] Yi Huang, Jiancheng Huang, Jianzhuang Liu, Mingfu Yan, Yu Dong, Jiaxi Lv, Chaoqi Chen, and Shifeng Chen. Wavedm: Wavelet-based diffusion models for image restoration. *IEEE Transactions on Multimedia*, 26:7058–7073, 2024. 2

[15] Junjie Ke, Qifei Wang, Yilin Wang, Peyman Milanfar, and Feng Yang. Musiq: Multi-scale image quality transformer. In *Proceedings of the IEEE/CVF international conference on computer vision*, pages 5148–5157, 2021. 6

[16] Haoying Li, Yifan Yang, Meng Chang, Shiqi Chen, Huajun Feng, Zhihai Xu, Qi Li, and Yueling Chen. Srdiff: Single image super-resolution with diffusion probabilistic models. *Neurocomputing*, 479:47–59, 2022. 1, 2

[17] Yawei Li, Yuchen Fan, Xiaoyu Xiang, Denis Demandolx, Rakesh Ranjan, Radu Timofte, and Luc Van Gool. Efficient and explicit modelling of image hierarchies for image restoration. In *Proceedings of the IEEE/CVF Conference on Computer Vision and Pattern Recognition*, pages 18278–18289, 2023. 2

[18] Jie Liang, Hui Zeng, and Lei Zhang. Details or artifacts: A locally discriminative learning approach to realistic image super-resolution. In *Proceedings of the IEEE/CVF conference on computer vision and pattern recognition*, pages 5657–5666, 2022. 2, 7

[19] Bee Lim, Sanghyun Son, Heewon Kim, Seungjun Nah, and Kyoung Mu Lee. Enhanced deep residual networks for single image super-resolution. In *Proceedings of the IEEE conference on computer vision and pattern recognition workshops*, pages 136–144, 2017. 2

[20] Pengju Liu, Hongzhi Zhang, Kai Zhang, Liang Lin, and Wangmeng Zuo. Multi-level wavelet-cnn for image restoration. In *Proceedings of the IEEE conference on computer vision and pattern recognition workshops*, pages 773–782, 2018. 2

[21] Ze Liu, Yutong Lin, Yue Cao, Han Hu, Yixuan Wei, Zheng Zhang, Stephen Lin, and Baining Guo. Swin transformer: Hierarchical vision transformer using shifted windows. In *Proceedings of the IEEE/CVF international conference on computer vision*, pages 10012–10022, 2021. 4

[22] Wei Long, Xingyu Zhou, Leheng Zhang, and Shuhang Gu. Progressive focused transformer for single image super-resolution. In *Proceedings of the Computer Vision and Pattern Recognition Conference*, pages 2279–2288, 2025. 2, 4

[23] Anish Mittal, Rajiv Soundararajan, and Alan C Bovik. Making a “completely blind” image quality analyzer. *IEEE Signal processing letters*, 20(3):209–212, 2012. 6

[24] Brian B Moser, Stanislav Frolov, Federico Rau, Sebastian Palacio, and Andreas Dengel. Waving goodbye to low-res: A diffusion-wavelet approach for image super-resolution. In *2024 International Joint Conference on Neural Networks (IJCNN)*, pages 1–8. IEEE, 2024. 3

[25] Brian B Moser, Stanislav Frolov, Federico Rau, Sebastian Palacio, and Andreas Dengel. Dynamic attention-guided diffusion for image super-resolution. In *2025 IEEE/CVF Winter Conference on Applications of Computer Vision (WACV)*, pages 451–460. IEEE, 2025. 1

[26] Axi Niu, Kang Zhang, Trung X Pham, Jinqiu Sun, Yu Zhu, In So Kweon, and Yanning Zhang. Cdpmr: Conditional diffusion probabilistic models for single image super-resolution. *arXiv preprint arXiv:2302.12831*, 2023. 1

[27] Axi Niu, Trung X Pham, Kang Zhang, Jinqiu Sun, Yu Zhu, Qingsen Yan, In So Kweon, and Yanning Zhang. Acdmsr:

Accelerated conditional diffusion models for single image super-resolution. *IEEE Transactions on Broadcasting*, 70(2): 492–504, 2024. 1

[28] Nobuyuki Otsu. A threshold selection method from gray-level histograms. *IEEE Transactions on Systems, Man, and Cybernetics*, 9(1):62–66, 1979. 5

[29] Subir Kumar Parida, RS Sengar, Rajbabu Velmurugan, DC Kar, and Swati Hiremath. Lifting wavelet-guided diffusion model for efficient image super-resolution. In *2025 25th International Conference on Digital Signal Processing (DSP)*, pages 1–5. IEEE, 2025. 3

[30] Seung Ho Park, Young Su Moon, and Nam Ik Cho. Perception-oriented single image super-resolution using optimal objective estimation. In *Proceedings of the IEEE/CVF conference on computer vision and pattern recognition*, pages 1725–1735, 2023. 1, 2

[31] Dustin Podell, Zion English, Kyle Lacey, Andreas Blattmann, Tim Dockhorn, Jonas Müller, Joe Penna, and Robin Rombach. Sdxl: Improving latent diffusion models for high-resolution image synthesis. *arXiv preprint arXiv:2307.01952*, 2023. 2

[32] Robin Rombach, Andreas Blattmann, Dominik Lorenz, Patrick Esser, and Björn Ommer. High-resolution image synthesis with latent diffusion models. In *Proceedings of the IEEE/CVF conference on computer vision and pattern recognition*, pages 10684–10695, 2022. 2

[33] Shuyao Shang, Zhengyang Shan, Guangxing Liu, LunQian Wang, XingHua Wang, Zekai Zhang, and Jinglin Zhang. Resdiff: Combining cnn and diffusion model for image super-resolution. In *Proceedings of the AAAI Conference on Artificial Intelligence*, pages 8975–8983, 2024. 2

[34] Yanli Shi, Xianhe Zhang, Yi Jia, and Jinxing Zhao. Multi-scale adversarial diffusion network for image super-resolution. *Scientific Reports*, 15(1):11690, 2025. 1

[35] Ashish Vaswani, Noam Shazeer, Niki Parmar, Jakob Uszkoreit, Llion Jones, Aidan N Gomez, Łukasz Kaiser, and Illia Polosukhin. Attention is all you need. *Advances in neural information processing systems*, 30, 2017. 2

[36] Jianyi Wang, Kelvin CK Chan, and Chen Change Loy. Exploring clip for assessing the look and feel of images. In *Proceedings of the AAAI conference on artificial intelligence*, pages 2555–2563, 2023. 6

[37] Jianyi Wang, Zongsheng Yue, Shangchen Zhou, Kelvin CK Chan, and Chen Change Loy. Exploiting diffusion prior for real-world image super-resolution. *International Journal of Computer Vision*, 132(12):5929–5949, 2024. 1, 6

[38] Xintao Wang, Liangbin Xie, Chao Dong, and Ying Shan. Real-esrgan: Training real-world blind super-resolution with pure synthetic data. In *Proceedings of the IEEE/CVF international conference on computer vision*, pages 1905–1914, 2021. 7

[39] Yufei Wang, Wenhan Yang, Xinyuan Chen, Yaohui Wang, Lanqing Guo, Lap-Pui Chau, Ziwei Liu, Yu Qiao, Alex C Kot, and Bihan Wen. Sinsr: diffusion-based image super-resolution in a single step. In *Proceedings of the IEEE/CVF conference on computer vision and pattern recognition*, pages 25796–25805, 2024. 1, 6

[40] Zhou Wang, Alan C Bovik, Hamid R Sheikh, and Eero P Simoncelli. Image quality assessment: from error visibility to structural similarity. *IEEE transactions on image processing*, 13(4):600–612, 2004. 6

[41] Zhaoyang Wang, Dongyang Li, Mingyang Zhang, Hao Luo, and Maoguo Gong. Enhancing hyperspectral images via diffusion model and group-autoencoder super-resolution network. In *Proceedings of the AAAI Conference on Artificial Intelligence*, pages 5794–5804, 2024. 2

[42] Pengxu Wei, Ziwei Xie, Hannan Lu, Zongyuan Zhan, Qixiang Ye, Wangmeng Zuo, and Liang Lin. Component divide-and-conquer for real-world image super-resolution. In *European conference on computer vision*, pages 101–117. Springer, 2020. 6

[43] Rongyuan Wu, Lingchen Sun, Zhiyuan Ma, and Lei Zhang. One-step effective diffusion network for real-world image super-resolution. *Advances in Neural Information Processing Systems*, 37:92529–92553, 2024. 2, 6

[44] Rongyuan Wu, Tao Yang, Lingchen Sun, Zhengqiang Zhang, Shuai Li, and Lei Zhang. Seesr: Towards semantics-aware real-world image super-resolution. In *Proceedings of the IEEE/CVF conference on computer vision and pattern recognition*, pages 25456–25467, 2024. 6

[45] Shengke Xue, Wenyuan Qiu, Fan Liu, and Xinyu Jin. Wavelet-based residual attention network for image super-resolution. *Neurocomputing*, 382:116–126, 2020. 3

[46] Tao Yang, Rongyuan Wu, Peiran Ren, Xuansong Xie, and Lei Zhang. Pixel-aware stable diffusion for realistic image super-resolution and personalized stylization. In *European Conference on Computer Vision*, pages 74–91. Springer, 2024. 2

[47] Jinsu Yoo, Taehoon Kim, Sihaeng Lee, Seung Hwan Kim, Honglak Lee, and Tae Hyun Kim. Enriched cnn-transformer feature aggregation networks for super-resolution. In *Proceedings of the IEEE/CVF winter conference on applications of computer vision*, pages 4956–4965, 2023. 2

[48] Zongsheng Yue, Jianyi Wang, and Chen Change Loy. Resshift: Efficient diffusion model for image super-resolution by residual shifting. *Advances in Neural Information Processing Systems*, 36:13294–13307, 2023. 1, 2, 6

[49] Jiqing Zhang, Chengjiang Long, Yuxin Wang, Haiyin Piao, Haiyang Mei, Xin Yang, and Baocai Yin. A two-stage attentive network for single image super-resolution. *IEEE Transactions on Circuits and Systems for Video Technology*, 32(3): 1020–1033, 2021. 2

[50] Kai Zhang, Jingyun Liang, Luc Van Gool, and Radu Timofte. Designing a practical degradation model for deep blind image super-resolution. In *Proceedings of the IEEE/CVF international conference on computer vision*, pages 4791–4800, 2021. 7

[51] Richard Zhang, Phillip Isola, Alexei A Efros, Eli Shechtman, and Oliver Wang. The unreasonable effectiveness of deep features as a perceptual metric. In *Proceedings of the IEEE conference on computer vision and pattern recognition*, pages 586–595, 2018. 6

[52] Wenlong Zhang, Yihao Liu, Chao Dong, and Yu Qiao. Ranksrgan: Generative adversarial networks with ranker for

image super-resolution. In *Proceedings of the IEEE/CVF international conference on computer vision*, pages 3096–3105, 2019. [2](#)

[53] Xiang Zhang, Yulun Zhang, and Fisher Yu. Hit-sr: Hierarchical transformer for efficient image super-resolution. In *European Conference on Computer Vision*, pages 483–500. Springer, 2024. [2](#)

[54] Yulun Zhang, Yapeng Tian, Yu Kong, Bineng Zhong, and Yun Fu. Residual dense network for image super-resolution. In *Proceedings of the IEEE conference on computer vision and pattern recognition*, pages 2472–2481, 2018. [2](#)

[55] Yuehan Zhang, Bo Ji, Jia Hao, and Angela Yao. Perception-distortion balanced admm optimization for single-image super-resolution. In *European Conference on Computer Vision*, pages 108–125. Springer, 2022. [3](#)